Opto-Electronic Advances

CN 51-1781/TN ISSN (Print) 2096-4579 ISSN (Online) 2097-3993

Tunable compound eyes with coaxial lens-on-lens ommatidia for cooperative bi-focal imaging

Zhi-Juan Sun, Wei-Jian Zhong, Qing Cai*, Yi-Fan Lu, Chang-Xu Li, Dong-Dong Han and Yong-Lai Zhang*

Citation: Sun ZJ, Zhong WJ, Cai Q et al. Tunable compound eyes with coaxial lens-on-lens ommatidia for cooperative bi-focal imaging. *Opto-Electron Adv* **9**, 250197 (2026).

https://doi.org/10.29026/oea.2026.250197

Received: 31 July 2025; Accepted: 10 December 2025; Published online: 9 February 2026

Opto-Electronic Advances

Article

April 2026, Vol. 9, No. 4

Open Access

Tunable compound eyes with coaxial lens-on-lens ommatidia for cooperative bi-focal imaging

Zhi-Juan Sun[1], Wei-Jian Zhong[1], Qing Cai[2]*, Yi-Fan Lu[2,3], Chang-Xu Li[1], Dong-Dong Han[1] and Yong-Lai Zhang[1]*

Abstract: Compound eyes (CEs) offer a unique design paradigm for developing artificial micro-optical systems. However, current bionic CEs still fall significantly short of their insect counterparts in performance, particularly regarding ommatidial spatial arrangement, size distribution, visual field adaptability and environmental perception. Inspired by the CEs of Sympetrum frequens, we developed a tunable bionic CE with bi-focal ommatidia by integrating a flexible lens-on-lens (LoL) array with microfluidics, enabling simultaneous bi-focal imaging. The polydimethylsiloxane (PDMS) LoL array was fabricated through sequential processing steps, including femtosecond laser dual-modification of quartz glass, two-step wet etching, and soft lithography using the resulting glass template. Integration of this flexible LoL array with a microfluidic chip produced a tunable CE with bi-focal ommatidia, allowing liquid-pressure modulation of CE configurations. We systematically investigated the optical performance of both LoL ommatidia and the integrated CE, including bi-focal focusing/imaging properties, tunable field-of-view (FOV), large-FOV imaging, and moving target monitoring. This tunable CE with LoL ommatidia demonstrates significant potential for cutting-edge applications.

Keywords: compound eye; femtosecond laser processing; lens on lens; tunable imaging; microfluidic chip

DOI: 10.29026/oea.2026.250197 | CSTR: 32247.14.oea.2026.250197

Citation: Sun ZJ, Zhong WJ, Cai Q et al. Tunable compound eyes with coaxial lens-on-lens ommatidia for cooperative bi-focal imaging. *Opto-Electron Adv* **9**, 250197 (2026).

1 Introduction

Insect compound eyes (CEs) that consist of thousands of densely packed ommatidia on a hemispherical surface are highly efficient natural visual systems. The ommatidia typically arrange in a tight hexagonal pattern, and each ommatidium acts as an independent photosensitive unit for multi-vision imaging[1–3]. As a product of natural evolution, CEs inherently possess advantages such as a large field of view (FOV), high temporal resolution, and strong dynamic perception capabilities, providing a unique design paradigm for developing artificial micro-optical systems with comparable imaging capabilities[4–7]. Advanced imaging systems based on CEs can break through the limitations of traditional single-aperture imaging, and thus achieves both large FOV and efficient information acquisition simultaneously through a multi-aperture distributed acquisition and parallel processing mechanism[8–10]. This unique advantage offers innovative technical solutions for cutting-edge applications such as particle image velocimetry[11], robotic vision[12], and virtual endoscopy[13,14].

In recent years, with the development of micro/nanofabrication technologies[15], bionic CEs have been successfully manufactured through various top-down and bottom-up approaches, such as inkjet printing[16,17], photolithographic hot melting[18,19], two-photon photopolymerization (TPP)[20–22] and the transformation of planar microlens arrays (MLAs)[23–25]. Among different manufacturing strategies, laser enabled CEs shows unique advantages due to the controllability over CE profiles. As typical examples, Hu et al.[26] fabricated aspherical CEs with logarithmic profile ommatidia using femtosecond laser TPP technology, which suitably addressed the problem with respect to optoelectronic integration of CE with planar photodetector chip. Similarly, Zhu

Received: 31 July 2025

Accepted: 10 December 2025

Published online: 9 February 2026

[1]State Key Laboratory of Integrated Optoelectronics, JLU Region, College of Electronic Science and Engineering, Jilin University, Changchun 130012, China; [2]Department of Oral Implantology, School and Hospital of Stomatology, Jilin University, Changchun 130012, China; [3]Jilin Provincial Key Laboratory of Science and Technology for Stomatology Nanoengineering, Jilin University, Changchun 130012, China.

*Correspondence: Q Cai, E-mail: caiqing@jlu.edu.cn; YL Zhang, E-mail: yonglaizhang@jlu.edu.cn

et al.[27] fabricated ultra-compact CE with nonuniform ommatidia at different positions, enabling planar imaging. Zhang et al.[28] further advanced femtosecond laser TPP-based fabrication technology by developing a dynamic holographically shifted multifoci strategy. Additionally, Hua et al.[29] produced CEs with smooth surfaces *via* femtosecond laser engraving combined with an annealing process, achieving nanoscale precision in surface finishing, which demonstrates remarkable technical features. As a typical three-dimensional (3D) processing technology, femtosecond laser manufacturing[30–33] has broken through the limitations of traditional processes, significantly enhancing the designability and manufacturing freedom of CEs. Recently, tunable liquid lenses demonstrate distinct advantages over traditional solid lenses in terms of response speed, parameter tuning, and environmental adaptability, emerging as a promising way to develop CEs with tunable ommatidia[34–36]. Nevertheless, the fabrication of tunable liquid lens array on non-planar 3D substrates is still challenging. At present, despite significant progress, bionic CEs still fall short of natural insect CEs, particularly in visual field adaptability and environmental perception.

For instance, the CEs of Sympetrum frequens[37] feature distinct regional differentiation. Its dorsal ommatidia have larger facets, while the ventral ones are smaller. Functionally, the dorsal region shows peak short-wavelength sensitivity at 360 nm. Conversely, the ventral region exhibits broader spectral photosensitivity with dual response peaks at 360 nm and 520 nm. This sophisticated regional specialization enables full-environment adaptive vision. In contrast, most artificial CEs use a uniform ommatidial design. Consequently, they demonstrate significant limitations in environmental adaptability and spectral response capabilities. Mimicking dragonfly CEs by integrating ommatidia with varying sizes and focal lengths could theoretically address this issue[38]. Nevertheless, such a uniform ommatidial design inherently restricts the alignment orientation of different ommatidia, which inevitably results in a limited imaging range.

As an appealing alternative, the reports on lens-on-lens (LoL) structures have provided new insights for developing advanced CEs[39–44]. The LoL structure that consists of two lenses of different sizes stacked together can achieve bi-focal imaging through the synergistic cooperation of the two layers of lens. Theoretically, employing the LoL structure as ommatidia of CE systems can lead to a complete curved dual-focal surface, which consequently overcomes the issue in multi-focal CEs based on nonuniform ommatidia arranged in different regions. However, in addition to the increased aberrations and the light loss, the LoL-ommatidia CEs with bi-focal planes may generate dual data streams per ommatidium. Due to the lack of dynamic tuning abilities, the two distinct ommatidia systems cannot be employed simultaneously for bi-focal imaging, which restricts dynamic adaptation to objects of different distances. Currently, the development of tunable CEs with LoL ommatidia remains a big challenge.

In this paper, we proposed a tunable artificial CE with coaxial LoL ommatidia for simultaneous bi-focal imaging. First, large-area of concave LoL template had been fabricated using a combined method of femtosecond laser dual modification and continuous wet etching. Subsequently, a soft convex LoL array was fabricated via soft lithography using polydimethylsiloxane (PDMS). To form a tunable CE structure, the flexible PDMS LoL array was integrated with a microfluidic chip. In this way, the FOV of the CE and the relative positions of the LoL ommatidia can be tuned by regulating the volume of liquid injected into the cavity. Our tunable CE with LoL ommatidia holds great potential for large FOV and bi-focal imaging.

2 Experimental methods

2.1 Fabrication of concave LoL array template

Firstly, two-tiered hexagonal crater arrays in vertical configuration are fabricated on quartz glass using femtosecond laser pulses (1030 nm, 280 fs, 100 kHz) focused through an objective lens with a numerical aperture of 0.6. The bottom-layer array was fabricated within the quartz glass bulk (~20 μm underneath the surface) using a laser power of 0.48 mW. For the second layer, the laser beam was focused on the glass surface, and the laser power is increased to 2.13 mW. The laser-modified sample was submerged in a 10% hydrofluoric acid solution at ambient temperature for a two-stage wet etching. Upon completion of buffered HF wet etching, the laser-induced craters were structurally converted into concave LoL array.

2.2 Fabrication of convex PDMS LoL array

PDMS and curing agent were mixed at a mass ratio of 10∶1. To eliminate air bubbles, the mixture underwent centrifugation at 3000 rpm for 5 minutes. The degassed precursor was subsequently spin-coated onto a quartz template at 500 rpm for 10 seconds, followed by thermal curing in an oven at 90 °C for 30 minutes. Upon complete solidification, the PDMS structure was carefully peeled from the template, yielding the PDMS convex LoL array.

2.3 Fabrication of LoL-ommatidia CE

The PDMS LoL array was bonded to a microfluidic chamber with a circular reservoir, ensuring precise alignment between the LoL array and the microfluidic chip. Liquid PDMS precursor was then injected into the chamber through a Teflon tube. As the liquid pressure increased, the planar MLA gradually bulged to form a CE structure. The geometry of the LoL-ommatidia CE can be tuned by varying the volume of the PDMS precursor.

2.4 Characterization

The morphological characterization was conducted using a scanning electron microscope (SEM, JSM-7500, JEOL, Japan), while the three-dimensional topography was measured via a laser scanning confocal microscope (LSCM, OLS4100, Olympus, Japan). Optical images were acquired with an optical microscope (NIB410, Nexcope, China).

3 Results and discussion

3.1 Design and fabrication of tunable LoL-ommatidia CE

Some of the insect CEs that consist of numerous closely and intricately arranged ommatidia exhibit distinct regional differentiation characteristics. A prime example is the CEs of dragonflies (Fig. 1(a)). Each distinct region of their CEs performs specialized visual functions to achieve holistic

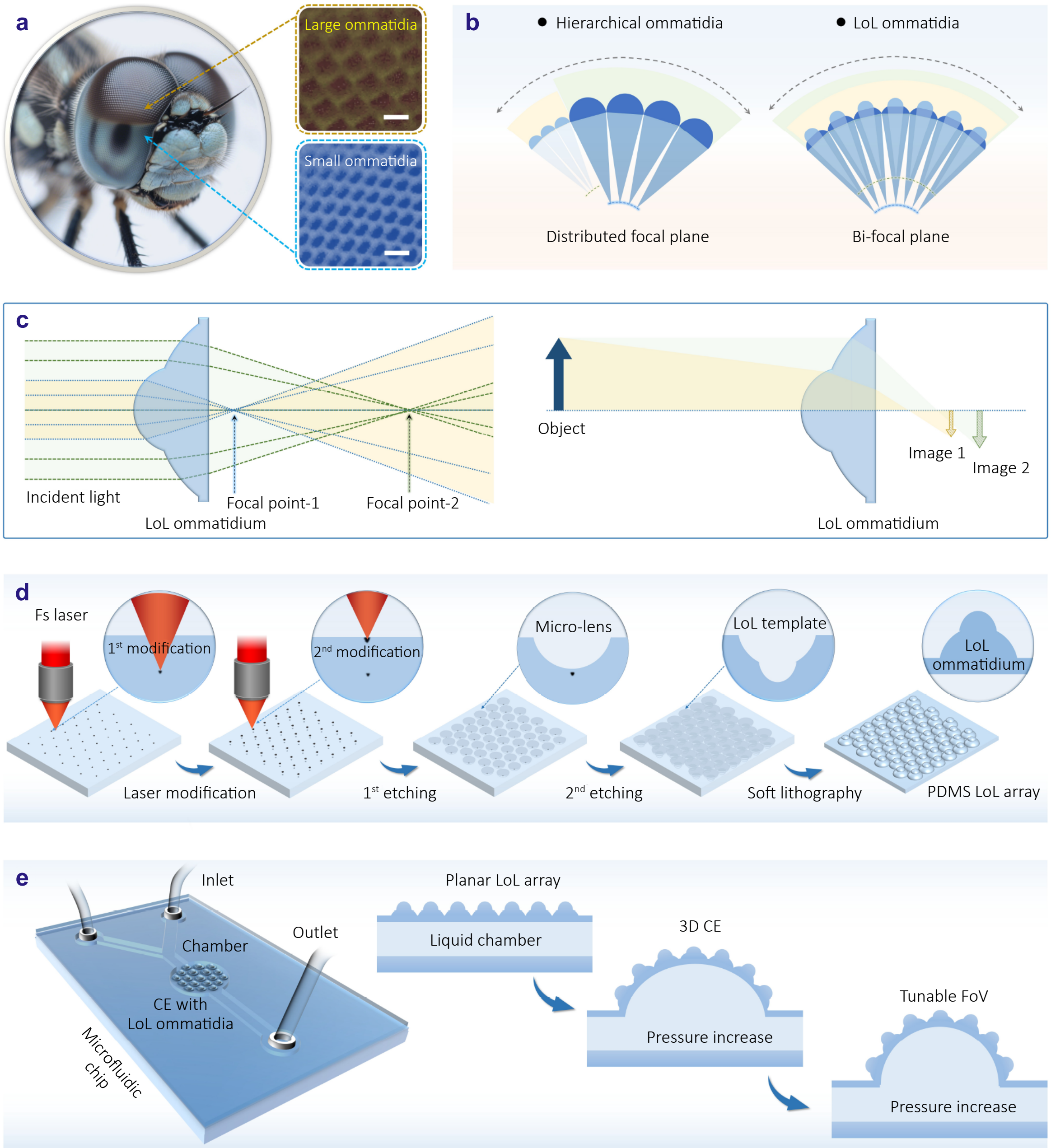

Fig. 1 | A schematic of the CE with LoL ommatidia. (a) The CE of dragonflies exhibit remarkable regional differentiation. Scale bars: 50 μm. (b) Two models of CE composed of hierarchical ommatidia and LoL ommatidia. (c) Schematic illustration of the imaging and focusing mechanism for the LoL ommatidium. (d) Fabrication process of the LoL array template. (e) A schematic of the fabrication of the LoL-ommatidia CE.

perception. However, for artificial CEs, such regional differentiation characteristics at the morphological level will give rise to serious problems. As shown in Fig. 1(b), the hierarchical ommatidia in segmented regions results in distributed focal planes, which restricts the orientation of all ommatidia. To address this limitation, we proposed a CE with LoL ommatidia. In this way, bi-focal plane imaging can be achieved throughout the FOV. The LoL ommatidium features coaxial convex lenses stacked vertically. Take advantage of the LoL structure, incident light can be focused onto two distinct focal planes (Fig. 1(c)). Consequently, an object can form two distinct images through the LoL ommatidium (Image 1 and Image 2, Fig. 1(c)). Unlike traditional zonal non-uniform CEs that tune image plane to match the planar sensor, the CEs with LoL ommatidia enable independent bi-focal imaging. By tuning the curvature of the base, the spatial positions of the two layers of lenses can be altered to match the planar sensor, and the FOV can be modulated simultaneously. The synergistic cooperation of the two lenses can promote the utilization of ommatidia and the environmental adaptability. To fabricate the LoL-ommatidia CEs, we developed a combined technology that involves femtosecond laser dual modification, two-step wet etching, soft lithography and microfluidic injection. As shown in Fig. 1(d), dual laser modification has been implemented to create two-tiered hexagonal crater arrays on quartz glass. The embedded crater array (20 μm underneath surface) and the surface crater array are fabricated successively. Then two-stage wet etching was implemented until the formation of concave LoL array that was further employed as a hard template for mass-production of PDMS LoL arrays via soft lithography.

Furthermore, to endow the CE structure with tunable FOV, the flexible PDMS LoL array is combined with a microfluidic chip, in which a liquid chamber is aligned underneath the planar PDMS LoL array. By injecting PDMS precursor into the reservoir, 3D CE structure with a hemispherical base gradually formed with the increase of liquid pressure (Fig. 1(e)). Interestingly, the FOV of the CE and the relative distribution of the LoL ommatidia can be precisely tuned within a certain range by varying the pressure. The integration of microfluidic chamber with LoL array also enables dynamic tunability, by which the configuration of the CE can be modulated in a controlled fashion. Notably, the relative spatial position of the LoL ommatidia can be precisely tuned to match the image sensor, thereby enhancing dynamic adaptability. Under certain conditions, the complementary dual focus data streams can be captured simultaneously at different regions. Nevertheless, the tunable FOV may bring additional difficulties for integration with planar CCD/CMOS detectors. In this regard, the development of flexible detectors might be a solution to this issue[4,45]. Unlike conventional zoom lenses with tunable magnification, the tunable FOV not only change the "view angle", but also alters the spatial distribution of the two sets of images formed by the LoL ommatidia, which significantly enhances the observation efficiency and scene compatibility in practical applications.

3.2 Characterization of the LoL template

The quartz glass concave LoL array was fabricated using a femtosecond laser dual-modification process followed by HF wet etching. During this process, the concave LoL structure evolved progressively through two distinct stages. The first stage corresponds to the formation of the initial surface concave lens, whereby the second stage commences upon etching into the embedded modified region and continues until the complete LoL structure is realized. In this work, we employed laser scanning confocal microscope (LSCM) to investigate the morphology evolution of the LoL structure throughout this process, and the relevant results are shown in Fig. 2.

Initially, the laser-modified region on the quartz glass surface can be etched readily due to its relatively high reactivity. As etching time increased, this region gradually transformed into a concave lens structure[46,47], with both the size and depth of the lens increasing to etching duration. The process transitioned to a second stage once the embedded modified region became exposed, during which the base concave lens continued expanding in size and depth while a secondary concave lens simultaneously began developing. Figure 2(a) correspondingly illustrates the surface morphology evolution across different etching durations. Figure 2(b) shows the SEM image of the LoL structures after 12 hours of etching. The cross-sectional profile evolution was systematically characterized at 30 minute intervals following the initial 9 h etching period (Fig. 2(c)). Analysis reveals progressively regularized small lens contours with extended etching duration. A three-dimensional surface profile after 12 h of etching confirms the developed concave LoL structure (Fig. 2(d)), exhibiting cross-sectional consistency with Fig. 2(c). Quantitative measurements demonstrate etching-time dependency for both lens components. Large lens depth increased from 9.9 μm to 10.6 μm with diameter expansion from 34.6 μm to 44.7 μm (Fig. 2(e)), while small lens depth grew from 6.3 μm to 9.1 μm alongside diameter increase from 8.9 μm to 20.3 μm (Fig. 2(f)). This accelerated morphological evolution stems from higher etching rates within laser-modified regions. Crucially, controlled etching duration enables precise tuning of the small-to-large lens area ratio, which increased from 0.06 to 0.20 between 9–12 h (Fig. 2(g)). In this study, the area ratio of the two lenses can be tuned by adjusting laser processing parameters and etching time. Nevertheless, to achieve reasonable imaging performance based on the two lenses simultaneously, we need to balance this area ratio. Herein, the suitable area ratio is around 0.2.

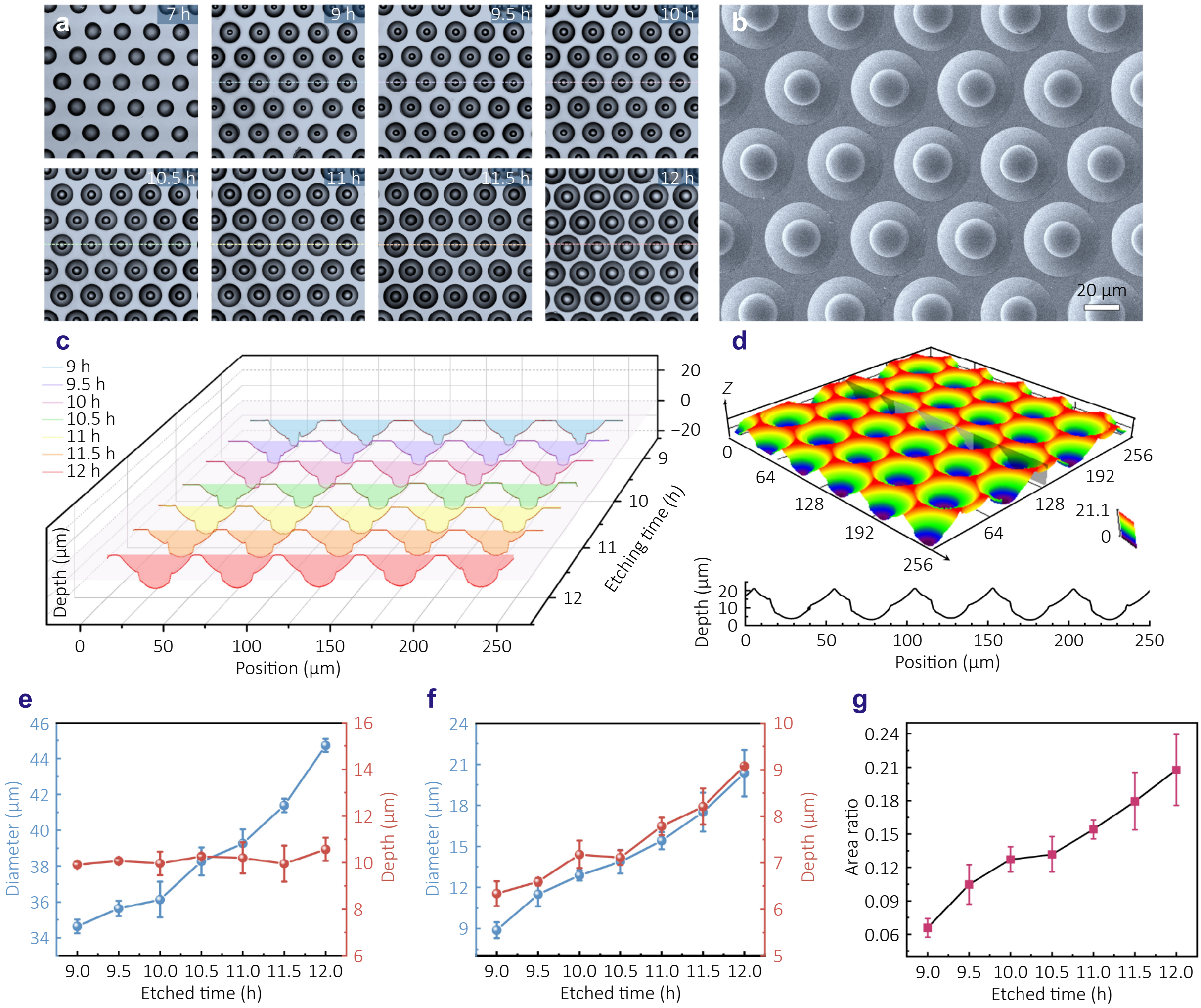

Fig. 2 | Morphological evolution of the concave LoL array template. (a) Morphological evolution of the concave LoL array during the wet etching process. (b) SEM images of the concave LoL array after etching for 12 h. (c) The cross-sectional profile of the LoL array extracted along the dashed line in (a). (d) 3D LSCM and cross-sectional morphology of the concave array template. (e, f) Dependence of diameters and heights of the large and small lenses with etching time, respectively. (g) Relationship between the area ratio of small lenses to large lenses and etching time.

3.3 Structural characterization of the LoL-ommatidia CE

The as-obtained concave LoL template has been employed to fabricate a flexible convex PDMS LoL array via soft lithography (Fig. 3(a)). After that the soft LoL array was combined with a microfluidic chip, and the tunable CE with LoL ommatidia formed. Structural consistency between the template and PDMS replica (Fig. 3(b)) was confirmed through CLSM imaging and cross-sectional profiling. The close-packed LoL array exhibits a 50 µm periodicity. Dimensional measurements indicate a large lens diameter of 52.32 µm and small lens dimension of 23.61 µm diameter. The total height of the LoL structure is ~20 µm. According to the parameters of the LoL structure, the radii of curvature of the large lens and the small lens are calculated to be 31.7 µm and 12.4 µm, respectively (Fig. S1). Accordingly, their focal lengths are 77.4 µm (large lens) and 30.3 µm (small lens), respectively. These results suggest that the focal planes of the two lenses are not overlapped. Figure 3(g) shows the SEM image of the entire LoL array, there are 1261 LoL ommatidia in approximately 2.6 mm^2. The magnified SEM image and the optical microscope images further demonstrates excellent structural uniformity (Fig. 3(d, e)).

By integrating the PDMS LoL array with a microfluidic chamber, the planar structure can be tuned to form a 3D CE structure by injecting PDMS precursor. The as-obtained CE is ~2 mm in diameter and 0.5 mm in height (Fig. 3(f)). Interestingly, the FOV of the CE that mainly depends on the surface curvature can be precisely tuned by increasing the volume progressively. Figure 3(g) shows the dependence of the curvature on the volume of PDMS precursor and the insets are photographs of their profiles at different volumes. Furthermore, the tuning process was repeated 15 times to demonstrate its repeatability (Fig. S2). In actual manufacturing, to ensure consistency during the tuning process, a

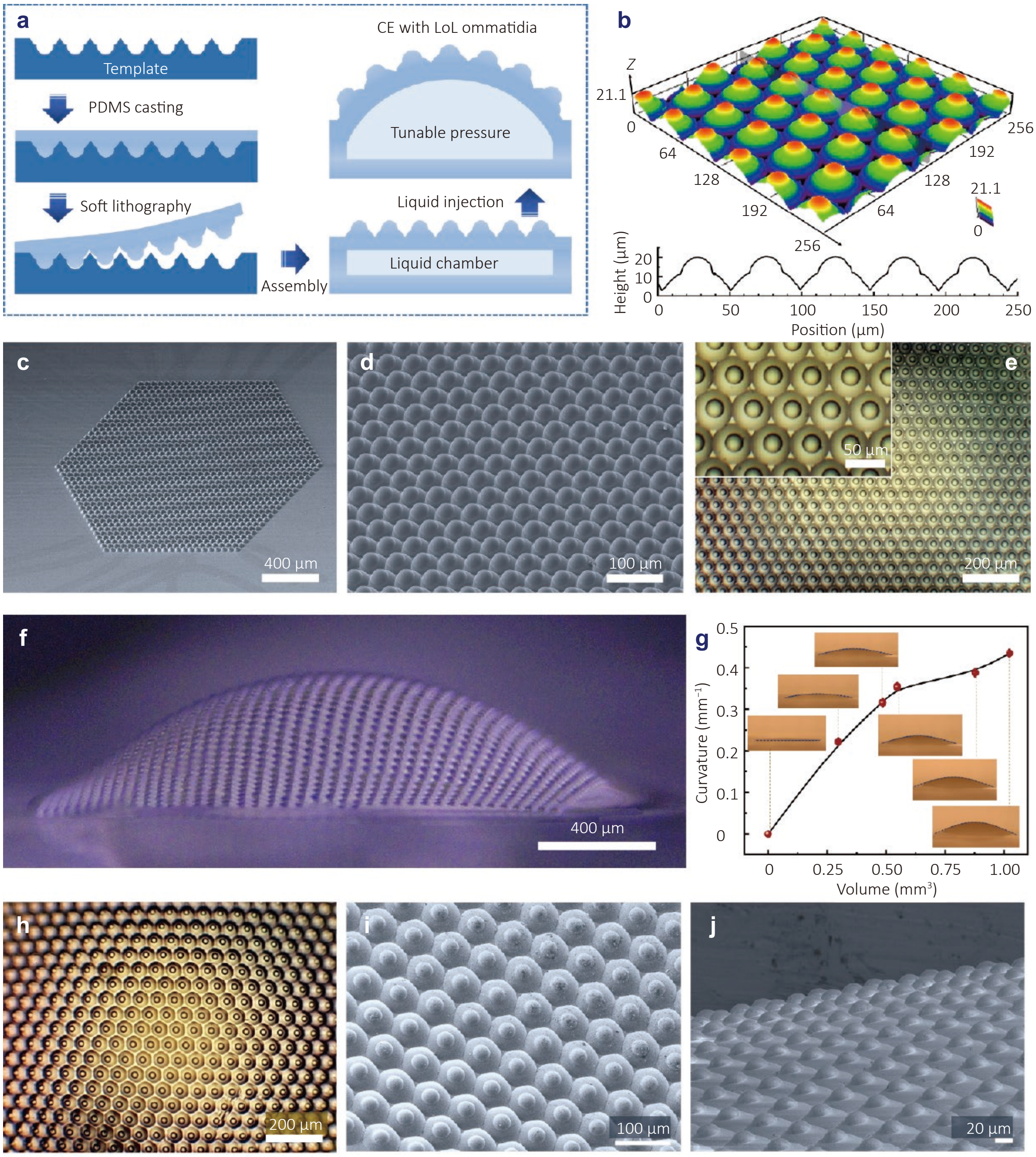

Fig. 3 | Fabrication and characterization of LoL-ommatidia CE. (a) Preparation process of the tunable CE. (b) 3D LSCM images and cross-sectional morphology of the PDMS convex LoL array. (c, d) SEM images of the PDMS convex LoL array. (e) Optical microscope images of the PDMS convex LoL array, the inset is the image of a magnified region. (f) Side-view optical microscope images of the tunable CE. (g) Correlation between the curvature of CE and the volume of the liquid chamber. (h) Optical microscope images of LoL-ommatidia CE. (i, j) SEM images of the local area of the LoL-ommatidia CE.

dependency relationship between the injected liquid volume and CE geometry should be established in advance, so that real-time observation of morphology evolution is not necessary. The maximum curvature of the prepared CEs is approximately 0.8 mm^{-1}. Figure 3(h) presents the top-view morphology of the CE, while Fig. 3(i, j) show its partial SEM images. Regional morphological details are shown in Fig. S3. Notably, during the formation of the CE, the LoL array had undergone significant stretching, which inevitably results in the morphology change. When the planar PDMS LoL array is transformed into a curved compound eye under liquid pressure, the film stretches under uneven stress, because the PDMS slice with LoL array is also uneven. Large lenses and their surrounding gaps (thin region) bear the main mechanical loads, which leads to a substantial increase in size. In contrast, small lenses (thick region) endure weaker direct stress and deform slightly. Additionally, the profiles of the LoL structure at different regions show that stretching at the edge is more obvious. The size of the large lens at the central region increased to 60.7 μm, and the lens size at the edge increased to 64.1 μm. The average size after stretching is ~62.4 μm. Accordingly, the average height of the LoL ommatidium decreased to 16.4 μm. Nevertheless, SEM images of the CE details show that the LoL structure maintain good morphology after such deformation. Nevertheless, the stretching of the LoL structure may slightly alter their focusing/imaging performance. With the increase of liquid pressure, the size of the lenses increased, whereas the heigh decreased. Accordingly, the focal length increased.

3.4 Optical performance

The imaging and focusing performance of both the planar LoL array and the resultant CE after deformation were characterized. In the case of planar LoL, both focal and image planes remain planar for both ommatidia types (Fig. S4). Upon deformation into a CE, these planes shifted to curved surfaces. Figure 4(d–f) demonstrates the focusing properties

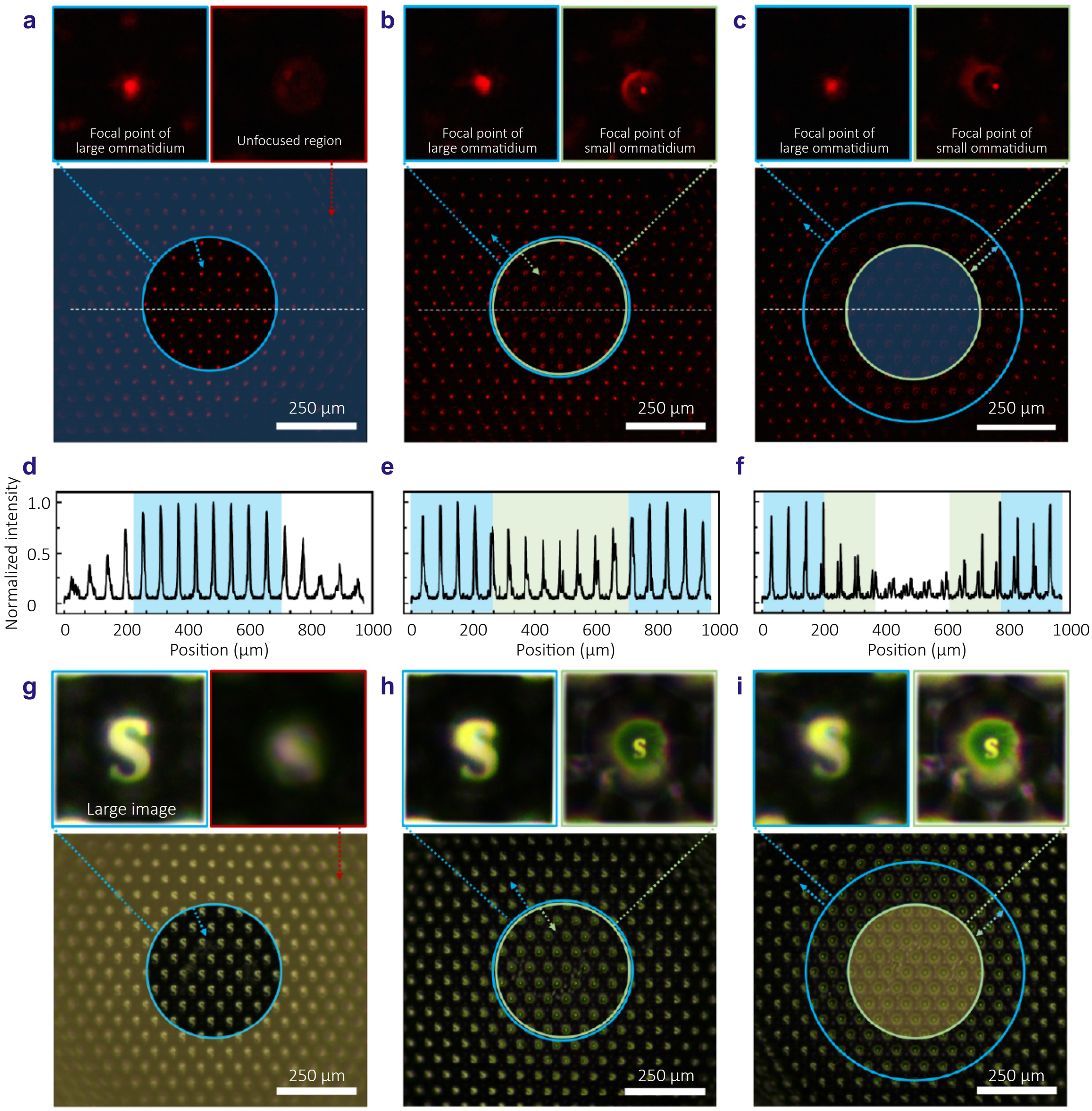

Fig. 4 | The focusing and imaging performances of the LoL-ommatidia CE. (a–c) The focusing results of LoL ommatidia in different regions. The insets are the focal spots of the large and small lenses. (d–f) The intensity distributions of the focal spots extracted along the dashed lines in (a), (b), and (c), respectively. (g–i) The imaging performance of a letter "S" by the LoL ommatidia in different regions of the CE. The insets are images formed by the large and small lenses.

of the LoL-ommatidia CE. When a laser beam vertically illuminated the CE, focal spots exhibited a dual-3D distribution (from both ommatidia types), preventing a planar CCD from capturing all spots simultaneously at fixed positions. By varying the relative position of CCD, clear focal spots from large and small ommatidia were captured across different regions.

Figure 4(d–f) show spot intensity distributions along the dashed lines in Fig. 4(a–c), with blue and green areas denoting effective focusing regions of large and small ommatidia, respectively. Initially, the CCD captured only central large ommatidia focal spots (Fig. 4(a)), while edge areas remained defocused. Figure 4(d) confirms intensity decay toward the periphery and central confinement of effective focusing. Adjusting the relative position enabled simultaneous capture of focal spots from central small ommatidia and peripheral large ommatidia (Fig. 4(b)), expanding the effective focusing area (Fig. 4(e)). Further adjustment defocused the center, allowing the CCD to capture focused spots from annular small ommatidia and far-peripheral large ommatidia (Fig. 4(c)), as validated by Fig. 4(f). For imaging tests, an S-shaped mask was employed as the object. Figure 4(g–h) show images from both ommatidia types, revealing a dual distribution pattern matching the focal spots. Distinct large and small "S" images were captured in different regions, as marked in Fig. 4(g–i). Notably, bright spots around the "S" images formed by the small ommatidia are observed due to the light convergence from the large ommatidia. To suppress this phenomenon, the focal length difference of the two lenses can be further modulated.

3.5 Tunable FOV

The FOV of the LoL-ommatidia CE was measured by adjusting the incident light angles. Light focused by the LoL ommatidia passes through the objective lens and is projected onto a CCD camera. The theoretical FOV formula is:

$$FOV = 2\arcsin\frac{2H \cdot r}{H^2 + r^2} , \tag{1}$$

where H denotes the height of the spherical base and r represents the base radius of the spherical cap. As mentioned previously, the curvature of CE can be tuned by varying the volume of PDMS precursor injected into the chamber. To demonstrate this FOV tunability, we tested two CEs with different curvatures. CE-1, with smaller curvature, had a diameter of 2.05 mm and a height of ~0.28 mm, while CE-2, with larger curvature, shared the same diameter (2.05 mm) but had a height of ~0.46 mm. Their theoretical FOVs were calculated as approximately 60° and 96°, respectively. For CE-1, focal spot distributions for both ommatidia types were captured at 0°, 10°, and 20° (Fig. 5(a, b)). For CE-2, distributions were tested at 0°, 20°, and 40° (Fig. 5(c, d)). Focal spots from both large and small ommatidia appear clear and bright, indicating good focusing properties. In our experiments, the maximum half FOV for the two CEs can reach 30° and 50°, respectively (Fig. S5), in good agreement with their theoretical values.

Additionally, point spread functions (PSFs) quantified the optical performance of the LoL ommatidia of CE-2. We first extracted and normalized the intensity of focal spots from the large ommatidia along the X-Y axis, plotting the distribution maps (Fig. 5(e, f)). The full width at half maximum (FWHM) values for these spots were 4.62 ± 0.44 μm (X-axis) and 4.53 ± 0.39 μm (Y-axis), with corresponding relative standard deviations (RSD) of approximately 9.52% and 8.61%, respectively. For comparison, focal spot intensity from the small ommatidia was also measured (Fig. 5(g, h)), yielding FWHM values of 2.01 ± 0.07 μm (X-axis, RSD: ~3.48%) and 2.09 ± 0.07 μm (Y-axis, RSD: ~3.35%). These results confirm that both ommatidia types exhibit good focusing ability within their theoretical FOV. The smaller RSD with respect to the small ommatidia indicates the better focusing performance, which may be attributed to the stretching of large ommatidia during the formation of CE.

3.6 Large FOV imaging

In lens optics, when objects are excessively large or positioned too close, edge rays become blocked causing vignetting, where image edges darken or disappear. This represents a typical FOV limitation. While CEs generally address FOV constraints effectively, the obtained image arrays from different ommatidia typically exhibit curved distributions, preventing simultaneous capture of all images. The CE with LoL ommatidia partially ameliorates this issue. As shown in Fig. 6(a), targets labeled "N, S, W, E, and C" were created for large-FOV imaging. The mask pattern is illustrated in Fig. 6(b), in which letter "C" is approximately 480 μm in size, and the other letters are approximately 200 μm in size. With the mask center aligned to the CE center, the central region received light from "C" while peripheral regions captured other letters. Keeping the mask and CE stationary while varying the receiving angle allowed full image capture (Fig. S6). The merged image shows inverted letter images (Fig. 6(c)). By leveraging the LoL ommatidia, all letters become observable. Notably, the images of "C" formed through small ommatidia appear diminutive, whereas other letters formed through large ommatidia. After extracting individual letter images, the large-FOV image was reconstructed according to their respective positions. The reconstructed image shows strong consistency with the target object (Fig. 6(d)), demonstrating its potential for large-FOV imaging.

3.7 Dynamic target detection

Beyond large-FOV imaging, the CE with LoL ommatidia also enables dynamic target detection. To validate this capability, we first imaged moving targets using individual large

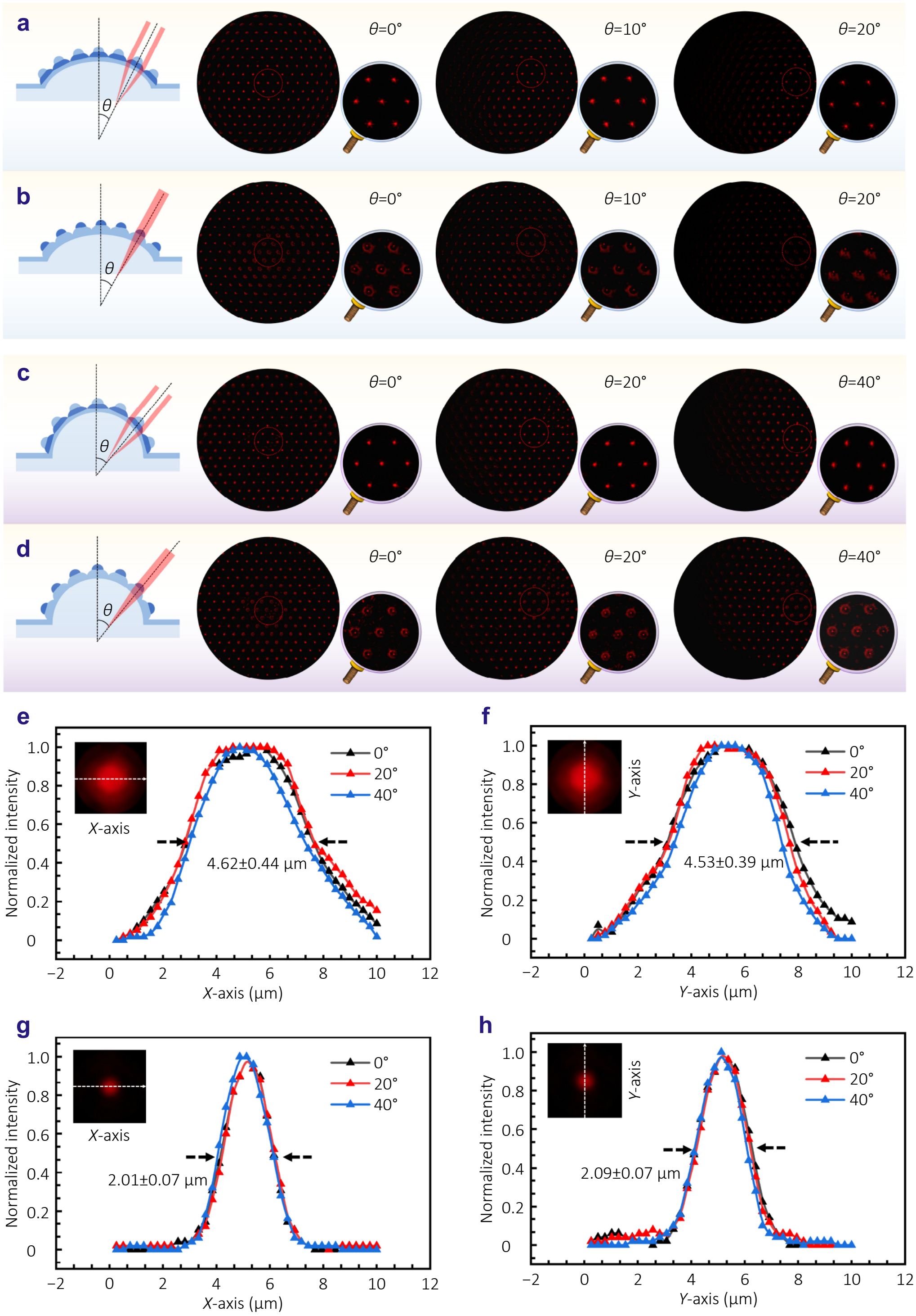

Fig. 5 | The tunable FOV of the LoL-ommatidia CE. (a, b) Focusing performance of large and small lenses of CE-1 under incident light at 0°, 10°, and 20°, respectively. (c, d) Focusing performance of large and small ommatidia of CE-2 under incident light at 0°, 20°, and 40°, respectively. (e–h) Normalized intensities extracted along the *X*-axis and *Y*-axis of the focal spots under different incident angles, in which (e, f) correspond to large lenses, (g, h) correspond to the small lenses of the LoL ommatidium.

and small ommatidia separately (Fig. 7(a)). Subsequently, collaborative detection experiments employing both large and small ommatidia were conducted (Fig. 7(b)). This approach allowed reconstruction of the target's moving trajectory from the acquired images. Notably, when the target is distant from the CE, either the large or small ommatidia system can be used for imaging. Figure 7(c) and 7(d) display images of a triangular target captured at eight

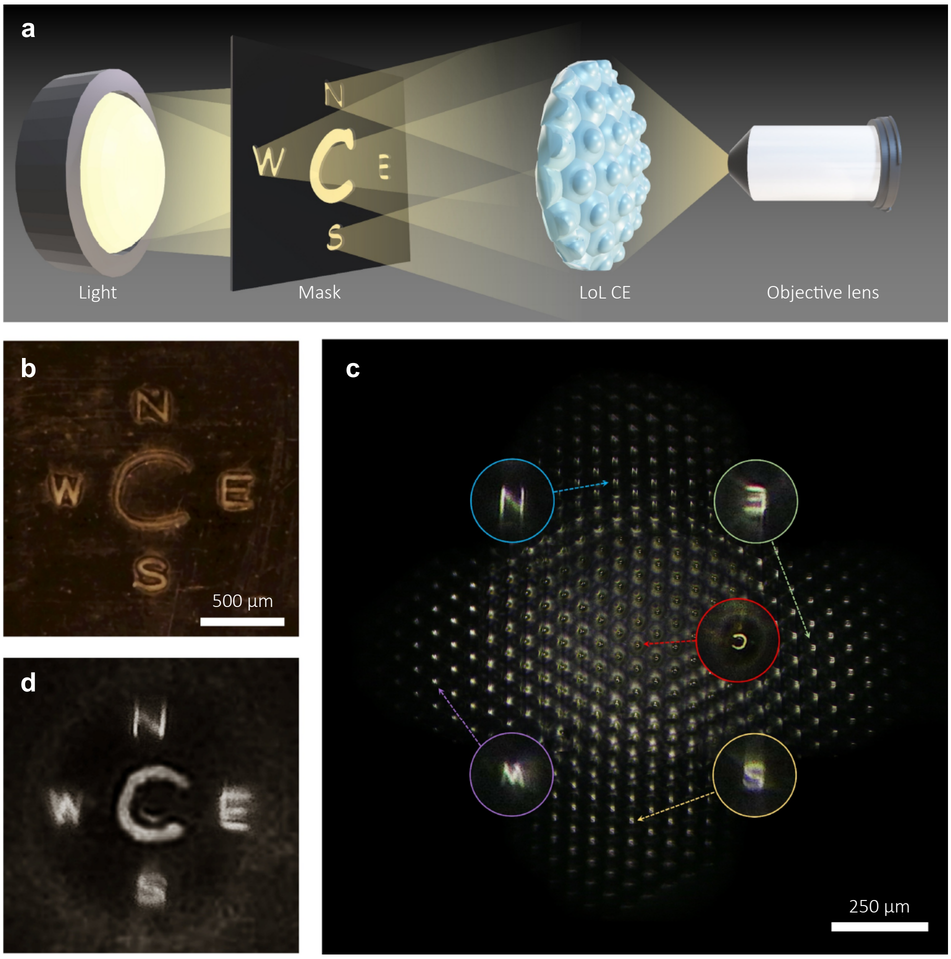

Fig. 6 | Large-FOV imaging performance of the LoL-ommatidia CE. (a) Schematic diagram of the imaging setup. (b) Optical microscopic image of the target mask. (c) Result of the imaging of the target object by the LoL-ommatidia CE. (d) Reconstructed image of the target object.

positions along its movement trajectory using the large and small ommatidia systems, respectively. As the target moved randomly, its spatial position changed. Consequently, images at different times were sequentially captured across different regions of the CE, with the image size reflecting the target distance. Using these sequential images, we calculated the target's relative position to reconstruct its moving trajectory. In Fig. 7(f), the yellow and black trajectories correspond to results from the large and small ommatidium systems, respectively, with the color bar indicating object-to-CE distance. Crucially, both the trajectories and distances reconstructed from the two systems show high consistency.

When the target distance changes significantly, individual ommatidium systems cannot capture target images. Consequently, collaboration between both types of ommatidia becomes essential. In this experiment, we used a dragonfly-shaped pattern as a moving target. Images at different time points were sequentially captured using both large and small ommatidia (Fig. 7(e)). As the dragonfly target first approached and then moved away from the CE, images were captured by large and small ommatidia at different regions of the CE. Based on these sequential images, we generated a position map (Fig. 7(g)) and a 3D coordinate map (Fig. 7(h)), revealing a movement trajectory from distant to near and then gradually away. These results clearly demonstrate the moving object detection and tracking capabilities of the LoL-ommatidia CE.

4 Conclusions

In conclusion, we developed a tunable CE with coaxial LoL ommatidia by integrating a planar LoL array with a microfluidic chip, enabling tunable FOV and cooperative bi-focal imaging. A quartz glass concave LoL template (approximately 2.6 mm^2 in area) was fabricated through combined femtosecond laser dual-modification and two-step wet etching. Using this template, we fabricated a flexible PDMS LoL array via soft lithography. Subsequent integration of the LoL array with a microfluidic chamber produced the tunable CE. Featuring a complete curved bi-focal plane, the CE with LoL ommatidia overcomes the limitations of both traditional single-focal-plane CEs and those with regionalized

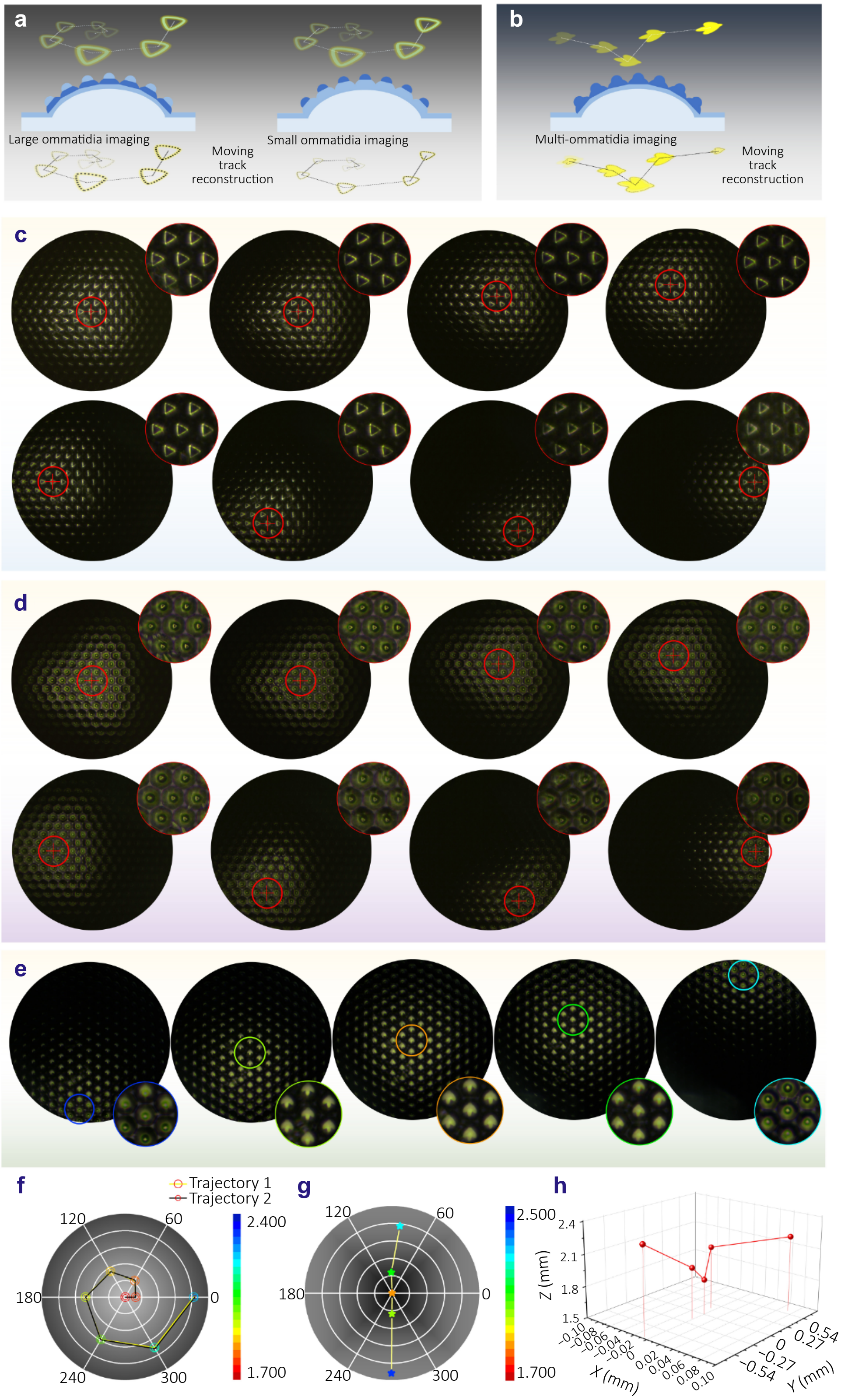

Fig. 7 | Detection of moving targets by the LoL-ommatidia CE. (a) Schematic diagram of target detection based on the large- and small-ommatidium systems individually. (b) Schematic diagram of target detection based on the cooperation of both large- and small-ommatidium systems. (c, d) Images of the triangular target at different positions captured by the large- and small-ommatidium systems, respectively. (e) Images of the dragonfly target at different positions captured collaboratively by the large- and small-ommatidium systems. (f) Trajectories of the triangular target derived from both large- and small-ommatidium systems. (g) Trajectory of the dragonfly target. (h) Moving path of the dragonfly target in a 3D coordinate system.

nonuniform ommatidia. Notably, cooperative bi-focal imaging was achieved by regulating the FOV and relative positions of different LoL ommatidia through controlled injection of PDMS precursor. Optical characterization confirmed the LoL-ommatidia CE's excellent bi-focal imaging capability, with both large and small ommatidia maintaining stable focusing performance within their theoretical FOVs. Furthermore, the dual focal planes of the LoL structure enable simultaneous large-FOV imaging and moving target monitoring. The collaborative imaging capability inherent to the LoL ommatidia also facilitates efficient moving target detection. This LoL-ommatidia CE holds significant promise for tunable, high-efficiency, large-FOV imaging applications.

References

1. Yagi N. A new type of compound eye. *Nature* **201**, 527 (1964).
2. Schoenemann B, Pärnaste H, Clarkson ENK. Structure and function of a compound eye, more than half a billion years old. *Proc Natl Acad Sci USA* **114**, 13489–13494 (2017).
3. Currea JP, Sondhi Y, Kawahara AY et al. Measuring compound eye optics with microscope and microCT images. *Commun Biol* **6**, 246 (2023).
4. Song YM, Xie YZ, Malyarchuk V et al. Digital cameras with designs inspired by the arthropod eye. *Nature* **497**, 95–99 (2013).
5. Stöckl A, Grittner R, Taylor G et al. Allometric scaling of a superposition eye optimizes sensitivity and acuity in large and small hawkmoths. *Proc R Soc B Biol Sci* **289**, 20220758 (2022).
6. Wu Q, Zhang SS, Liao WX et al. Heterogeneous compound eye camera for dual-scale imaging in a large field of view. *Opt Express* **30**, 45143–45155 (2022).
7. Gutiérrez D, Rigosi E, Nagloo N et al. Spatial resolution and optical sensitivity in the compound eyes of two common European wasps, *Vespula germanica* and *Vespula vulgaris*. *J Exp Biol* **227**, jeb246670 (2024).
8. Wang YY, Shi CY, Xu HR et al. A compact bionic compound eye camera for imaging in a large field of view. *Opt Laser Technol* **135**, 106705 (2021).
9. Liu SB, Xie BK, Yuan RY et al. Deep learning enables parallel camera with enhanced- resolution and computational zoom imaging. *PhotoniX* **4**, 17 (2023).
10. Zhang L, Zhan HY, Liu XY et al. A planar compound eye based microsystem for high precision 3D perception. *PhotoniX* **5**, 21 (2024).
11. Xu MX, Wu XB, Zhang Z et al. Compound-eye imaging imitation-based whole-field flow measurement. *Comput Electr Eng* **92**, 107141 (2021).
12. Zhou Y, Sun ZB, Ding YC et al. An ultrawide field-of-view pinhole compound eye using hemispherical nanowire array for robot vision. *Sci Robot* **9**, eadi8666 (2024).
13. Cogal O, Leblebici Y. An insect eye inspired miniaturized multi-camera system for endoscopic imaging. *IEEE Trans Biomed Circuits Syst* **11**, 212–224 (2017).
14. Sun JW, Kuschmierz R, Katz O et al. Lensless fiber endomicroscopy in biomedicine. *PhotoniX* **5**, 18 (2024).
15. He SK, Tian Y, Zhou HM et al. Review for micro-nano processing technology of microstructures and metadevices. *Adv Funct Mater* **35**, 2420369 (2025).
16. Zhang QS, Schambach M, Schlisske S et al. Fabrication of microlens arrays with high quality and high fill factor by inkjet printing. *Adv Opt Mater* **10**, 2200677 (2022).
17. Zhou SY, Guo H, Qian B et al. Single-step inkjet printing PDMS microlens arrays for tunable-focus artificial compound eyes. *Adv Mater Technol* **10**, 2400016 (2025).
18. Luo JS, Guo YC, Wang X et al. Design and fabrication of a multi-focusing artificial compound eyes with negative meniscus substrate. *J Micromech Microeng* **27**, 045011 (2017).
19. Bae SI, Kim K, Yang S et al. Multifocal microlens arrays using multilayer photolithography. *Opt Express* **28**, 9082–9088 (2020).
20. Jing X, Wang KX, Zhu RX et al. Design and fabrication of double-layer curved compound eye via two-photon polymerization. *IEEE Photonics Technol Lett* **33**, 231–234 (2021).
21. Jing X, Zhu RX, Wang KX et al. Transverse additive manufacturing and optical evaluation of miniature thin lenses in ultracompact micro multi-spherical compound eye. *Opt Lasers Eng* **151**, 106913 (2022).
22. Wang ZH, Wu YL, Chen L et al. Spatial light assisted femtosecond laser direct writing of a bionic superhydrophobic Fresnel microlens arrays. *Opt Laser Technol* **180**, 111451 (2025).
23. Deng ZF, Chen F, Yang Q et al. Dragonfly-eye-inspired artificial compound eyes with sophisticated imaging. *Adv Funct Mater* **26**, 1995–2001 (2016).
24. Xu Q, Dai B, Jiao ZA et al. Fabrication of large micro-structured high-numerical-aperture optofluidic compound eyes with tunable angle of view. *Opt Express* **26**, 33356–33365 (2018).
25. Li J, Wang WJ, Mei XS et al. Artificial compound eyes prepared by a combination of air-assisted deformation, modified laser swelling, and controlled crystal growth. *ACS Nano* **13**, 114–124 (2019).
26. Hu ZY, Zhang YL, Pan C et al. Miniature optoelectronic compound eye camera. *Nat Commun* **13**, 5634 (2022).
27. Zhu L, Liu YQ, Wan JY et al. Ultra-compact on-chip camera based on optoelectronic compound eyes with nonuniform ommatidia. *Int J Extrem Manuf* **7**, 015502 (2025).
28. Zhang LR, Liu BR, Wang CW et al. Functional shape-morphing microarchitectures fabricated by dynamic holographically shifted femtosecond multifoci. *Nano Lett* **22**, 5277–5286 (2022).
29. Hua JG, Liang SY, Chen QD et al. Free-form micro-optics out of crystals: femtosecond laser 3D sculpturing. *Adv Funct Mater* **32**, 2200255 (2022).
30. Tan JW, Wang G, Li YF et al. Femtosecond laser fabrication of refractive/diffractive micro-optical components on hard brittle materials. *Laser Photonics Rev* **17**, 2200692 (2023).
31. Zheng JX, Tian KS, Qi JY et al. Advances in fabrication of micro-optical components by femtosecond laser with etching technology. *Opt Laser Technol* **167**, 109793 (2023).
32. Liu YA, Ding Y, Liu ZP et al. Ultrafast laser one-step construction of 3D micro-/nanostructures achieving high-performance zinc metal anodes. *PhotoniX* **5**, 6 (2024).
33. Gao L, Zhang QM, Gu M. Femtosecond laser micro/nano processing: from fundamental to applications. *Int J Extrem Manuf* **7**, 022010 (2025).
34. Liu C, Zheng Y, Wang D et al. Multi-wavelength achromatic 3D meta-holography with zoom function. *Adv Sci* **12**, 2501881 (2025).
35. Zheng Y, Lu XK, Li JN et al. Adaptive compound eye imaging device based on electrowetting liquid aperture with adjustable shape. *Adv Intell Syst* **7**, e202500412 (2025).
36. Zheng Y, Zhang HR, Li XW et al. Fast-zoom and high-resolution sparse compound-eye camera based on dual-end collaborative optimization. *Opto-Electron Adv* **8**, 240285 (2025).
37. Futahashi R, Kawahara-Miki R, Kinoshita M et al. Extraordinary diversity of visual opsin genes in dragonflies. *Proc Natl Acad Sci USA* **112**, E1247–E1256 (2015).
38. Luan SY, Cao H, Deng HF et al. Artificial hyper compound eyes enable variable-focus imaging on both curved and flat surfaces. *ACS Appl Mater Interfaces* **14**, 46112–46121 (2022).
39. Yu HB, Zhou GY, Chau FK et al. A liquid-filled tunable double-focus microlens. *Opt Express* **17**, 4782–4790 (2009).
40. Lee JM, Lee D, Baek Y. Fabrication of dual-focus dual-layered microlens. *Opt Commun* **289**, 69–74 (2013).
41. Yang Q, Tong SY, Chen F et al. Lens-on-lens microstructures. *Opt*

Lett **40**, 5359–5362 (2015).
42. Huang YY, Zhao R, Miao WH et al. A bifocal compound liquid lens with continuous zoom based on selective wettability. *Opt Lett* **47**, 3824–3827 (2022).
43. Zhou Y, Kuang FL, Li R et al. Bifocal flat lens with different imaging characteristics for a dual-sensor imaging system. *Sci Rep* **12**, 18996 (2022).
44. Zhang X, Wang L, Cao XW et al. Single femtosecond pulse writing of a bifocal lens. *Opt Lett* **49**, 911–914 (2024).
45. Zheng D, Xie ZQ, Huang W et al. Ultra-flexible pixelated perovskite photodetectors enabled by honeycomb polymer grids for high-resolution imaging. *Adv Mater* **37**, 2415068 (2025).
46. Chen F, Liu HW, Yang Q et al. Maskless fabrication of concave microlens arrays on silica glasses by a femtosecond-laser-enhanced local wet etching method. *Opt Express* **18**, 20334–20343 (2010).
47. Zhou WJ, Li R, Li M et al. Fabrication of microlens array on chalcogenide glass by wet etching-assisted femtosecond laser direct writing. *Ceram Int* **48**, 18983–18988 (2022).

Acknowledgements

This work was supported by National Key Research and Development Program of China under Grant No. 2022YFB4600400; the National Natural Science Foundation of China under Grant Nos. T2325014 and 62275100; The Natural Science Foundation of Jilin Province under Grant No. 20230101350JC.

Author contributions

All authors commented on the manuscript. Zhi-Juan Sun completed the fabrication of CE, paper writing, experimental data collection, and drawing. Dong-Dong Han helped for experimental data analysis. Wei-Jian Zhong provided assistance with the wet etching process. Yi-Fan Lu provided assistance with bionic modeling. Chang-Xu Li contributed to the optimization of laser processing platform. Yong-Lai Zhang and Qing Cai proposed the original idea and supervised the project.

Competing interests

The authors declare no conflicts of interest.

Data availability

The data that support the findings of this study are available from the corresponding author upon reasonable request.

Supplementary information

Supplementary information for this paper is available at https://doi.org/10.29026/oea.2026.250197

Published by Editorial Office of *Opto-Electronic Advance*, Institute of Optics and Electronics, Chinese Academy of Sciences.